Electron response in gyrofluid simulations of magnetic reconnection

Journal of Physics: Conference Series **260** (2010) 012015 doi:10.1088/1742-6596/260/1/012015

Electron response in gyrofluid simulations of magnetic reconnection

A Perona[1,3], D Grasso[2,1] and D Borgogno[1]

[1] Burning Plasma Research Group, Dip. di Energetica, Politecnico di Torino, Italy
[2] Istituto dei Sistemi Complessi-CNR, Roma, Italy

E-mail: anna.perona@polito.it

Abstract. We investigate the behaviour of an electron population during the evolution of a spontaneous collisionless magnetic reconnection event, reproduced by a two-dimensional version of a Hamiltonian gyrofluid model. This model can be applied in electromagnetic problems where nonlinear effects are important, such as the sawtooth crash in the core of fusion devices. The electron dynamics in the presence of the reconnection fields is reconstructed by means of a test particle code, based on a relativistic Hamiltonian guiding centre formulation of the electron motion. The moments of the electron distribution function and the effects determined by the peculiar structure of the parallel electric field on the electron temperature in the reconnection region are reconstructed and compared with the corresponding quantities evolved by the fluid reconnection model.

1. Introduction

One of the main features of magnetic reconnection is that a local relaxation of the topological magnetic structure is accompanied by a local fast release of magnetic energy, that can be converted into heating of the plasma and particle acceleration. Thermal electrons can be accelerated by the strong electric fields formed during magnetic reconnection, thus becoming suprathermal or even relativistic [1]. Electron acceleration following sawtooth crashes and disruptions has been observed in laboratory tokamak experiments [2], [3], as well as during solar flares [4] and in diffusion regions of the Earth's magnetotail [5]. The theoretical and numerical investigation of the electron acceleration mechanism has considered various models of magnetic reconnection in different parameter regimes [6], [7], [8], [9], [10]. As these works have pointed out, the structure and, when considered, the evolution of the reconnection electric field play a significant role in determining the energy and the amount of energetic electrons generated.
In the rarefied, high temperature plasmas that characterize many configurations of interest, collisions are so rare that they do not represent an efficient mechanisms for breaking the magnetic field lines. Moreover, the electron-ion collision time can be longer than the observed relaxation time as is the case, for instance, of sawtooth crashes occurring in Tokamak esperiments.
In a fluid representation of magnetic reconnection in such collisionless plasmas, the finite electron mass can account for reconnection on so fast relaxation times (see [11] and references therein).

[3] Present address: Dipartimento di Energetica, Politecnico di Torino, corso Duca degli Abruzzi 24, 10138 Torino, Italy

In our work, we reconstruct the response of a population of thermal electrons to the fields characterizing an inertial magnetic reconnection process where a strong guide field is present. This process is described by a gyrofluid model where finite ion Larmor radius effects are retained. The resulting electric field exhibits a structure considerably different with respect to the electric field arising in the two-fluid, cold-ion model that represents the limit of the gyrofluid model for $\rho_i \to 0$ [12], [13]. In the cold-ion limit, the parallel electric field has a monopole structure, peaked in the X-point region, that significantly accelerates the electrons during the nonlinear phase of the process, although even at this stage neither highly energetic nor relativistic tails are observed in the electron distribution function [14]. Aim of our investigation is to determine whether a more significant amount of energetic electrons is generated by the finite-ρ_i electric field and how the electron distribution function and the kinetic moments are distorted with respect to the corresponding fluid quantities.
The gyrofluid model of magnetic reconnection and the equations reproducing the dynamics of the electron guiding centers in the presence of the reconnection fields are introduced in Section 2 and in Section 3, respectively. The results of the numerical simulations performed with the code where these equations have been implemented are presented in Section 4. Finally, conclusions are drawn in Section 5.

2. The gyrofluid reconnection model

In our investigation, we follow the evolution of the reconnection fields evolved by a Padé approximant version of a Hamiltonian gyrofluid model introduced in Ref. [15]. This model, that has been investigated in Ref. [16], can describe both the "inertial" ($\beta_e \ll m_e/m_i$) and the "kinetic" ($\beta_e \gg m_e/m_i$) regimes of the Alfvén wave (β_e is the ratio of the electron kinetic pressure to the magnetic pressure) and extends the models adopted in Refs. [17] and [18] by additionally evolving the ion guiding center density. In particular, we focus on a two-dimensional configuration, where the effects related to the curvature of the magnetic field lines and the dependence of the fields on z are neglected. The density of the ion guiding centers, n_i, the electron density, n_e, and the magnetic flux, $\psi = A_z$, are evolved according to the equations

$$\frac{\partial n_i}{\partial t} + [\Phi, n_i] = 0 \,, \tag{1}$$

$$\frac{\partial n_e}{\partial t} + [\phi, n_e] - [\psi, \nabla^2 \psi] = 0 \,, \tag{2}$$

$$\frac{\partial (\psi - d_e^2 \nabla^2 \psi)}{\partial t} + [\phi, \psi - d_2^2 \nabla^2 \psi] + \rho_s^2 [\psi, n_e] = 0 \,, \tag{3}$$

where A_z is the $z-$component of the vector potential, $\rho_s = \sqrt{T_e m_i/(eB^2)}$ is the sound Larmor radius, related to the electron temperature, T_e, $d_e = \sqrt{m_e/(\mu_0 n e^2)}$ is the electrons skin depth, ϕ is the electrostatic potential, $\Phi = 1/(1 - \rho_i^2 \nabla^2)\phi$ is the gyroaveraged electrostatic potential, $\rho_i = \sqrt{T_i/T_e}\rho_s$ is the ion Larmor radius, T_i, m_i and m_e represent the ion temperature, the ion and the electron masses, respectively, and $[A, B] = \mathbf{e}_z \cdot \nabla A \times \nabla B$. Moreover, the electron density is related to the ion density and to the electrostatic potential

$$n_e = \frac{n_i}{1 - \frac{\rho_i^2}{2}} + \frac{\nabla^2}{1 - \rho_i^2 \nabla^2} \phi \,. \tag{4}$$

Equations (1)-(4) have been normalized according to

$$(t, x, d_e, n_i, n_e, \psi, \phi) = (\frac{v_A}{L}\hat{t}, \frac{\hat{x}}{L}, \frac{\hat{d}_e}{L}, \frac{L}{\hat{d}_i}\frac{\hat{n}_i}{n_0}, \frac{L}{\hat{d}_i}\frac{\hat{n}_e}{n_0}, \frac{\hat{A}_z}{BL}, \frac{\hat{\rho}_s^2}{L^2}\frac{L}{d_i}\frac{e\hat{\phi}}{T_e}) \tag{5}$$

where $v_A = L/\tau_A$, L is the macroscopic scale length and $\tau_A = \sqrt{nM}L/B_{y0}$ is the Alfvén time. The fluid fields characterizing the magnetic reconnection process are calculated considering an equilibrium magnetic flux function, $\psi_{eq} = 0.1/\cosh^2 x$, unstable to perturbations around the rational surface located at $x = 0$ and chosen in such a way as to avoid too early cross-talking between magnetic islands. In particular, the analytical equilibrium flux function is approximated up to 11 modes by a truncated Fourier series, since we impose double periodic boundary conditions. The ion and the electron densities are assumed to be uniform at the equilibrium, and the temperatures for both the ions and the electrons are taken to be constant throughout the reconnection process. The initial perturbation is applied on the ion density, $\tilde{n_i} \propto \cos(x+y) - \cos(x-y)$.

3. The electron equations

The dynamics of the electron guiding centers in the presence of the reconnection fields has been reconstructed in the same geometry of the gyrofluid model introduced in Sec. 2. In order to take into account the eventuality of a very large increase in the electron velocity, we adopted a relativistic Hamiltonian formulation [19]. The unperturbed relativistic guiding-centre phase-space Lagrangian is expressed in terms of the guiding-centre coordinates as $L \equiv (p_{||}\mathbf{b} - e\mathbf{A}) \cdot \dot{\mathbf{R}} - \frac{m}{e}\mu\dot{\theta} - W$, where $\mathbf{b} = \mathbf{B}/B$, $p_{||} \equiv \mu_0\gamma\mathbf{v}\cdot\mathbf{b}$, $\gamma \equiv \sqrt{1 + (p_{||}^2 + p_\perp^2)/(m_0^2c^2)}$, $m \equiv m_0\gamma$, $\mathbf{R}$ denotes the guiding-centre position, $(p_{||}, \mu, \theta)$ are the guiding-centre momentum coordinates, and (t, W) are the guiding-centre time and energy coordinates. The usual procedure yields the equations of motion from the relativistic Hamiltonian, i.e.

$$\dot{y} = \partial H/\partial p_y \ , \qquad \dot{z} = \partial H/\partial p_z \ , \tag{6}$$

$$\dot{p_y} = -\partial H/\partial y \ , \qquad \dot{p_z} = -\partial H/\partial z \ , \tag{7}$$

where $H = \sqrt{p_{||}^2c^2 + 2\mu B m_0 c^2 + m_0^2c^4} - e\Phi$, $\mu = p_\perp^2/(2m_0B)$ is the magnetic momentum, $W = e\Phi$ is the energy, c is the speed of light, and the conjugate momenta to the y and z coordinates are given by

$$p_y = p_{||}b_y - eA_y \ , \qquad p_z = p_{||}b_z - eA_z \ . \tag{8}$$

The resulting set of equations describes the evolution in time of the $(x, y, p_{||})$ guiding-centre coordinates [14]

$$\dot{x} = \frac{1}{(b_y g_z - b_z g_y)}\{b_y[\dot{p}_z + e(\frac{\partial\tilde{\psi}}{\partial t} + \frac{\partial\tilde{\psi}}{\partial y}\dot{y}) - p_{||}(\frac{\partial b_z}{\partial t} + \frac{\partial b_z}{\partial y}\dot{y})] - b_z[\dot{p}_y - p_{||}(\frac{\partial b_y}{\partial t} + \frac{\partial b_y}{\partial y}\dot{y})]\} \ , \tag{9}$$

$$\dot{y} = \frac{p_{||}^2\frac{\partial b_z}{\partial x} - p_{||}e\frac{\partial A_z}{\partial x} - mb_z(\mu\frac{\partial B}{\partial x} - e\frac{\partial\Phi}{\partial x})}{m(g_z b_y - g_y b_z)} \ , \tag{10}$$

$$\dot{p}_{||} = \frac{1}{(b_y g_z - b_z g_y)}\{g_z\dot{p}_y - g_y\dot{p}_z + g_y[p_{||}(\frac{\partial b_z}{\partial t} + \frac{\partial b_z}{\partial y}\dot{y}) - e(\frac{\partial\tilde{\psi}}{\partial t} + \frac{\partial\tilde{\psi}}{\partial y}\dot{y})] - g_z p_{||}(\frac{\partial b_y}{\partial t} + \frac{\partial b_y}{\partial y}\dot{y})\} \ , \tag{11}$$

where the two quantities g_y and g_z are defined as

$$g_y = (p_{||}\frac{\partial b_y}{\partial x} - e\frac{\partial A_y}{\partial x}) \ , \qquad g_z = (p_{||}\frac{\partial b_z}{\partial x} - e\frac{\partial A_z}{\partial x}) \ .$$

and the components of the vector potential can be expressed in terms of the magnetic field components as $A_x = 0$, $A_y = B_0 x$, and $A_z = (\psi_{eq} + \tilde{\psi})$.

3.1. Kinetic moments in the δf approach

The behaviour of the electron guiding-centers has been reconstructed by means of a test particle code, where Eqs. (9)-(11) have been implemented and a Maxwellian distribution function has been assumed for the electrons at the equilibrium. We adopted a δf technique, which has the advantage of reducing the number of particles required in order to adequately fill the four-dimensional phase space $(x, y, p_{||}, p_{\perp})$ while resolving small fluctuation in the electron distribution function [20]. The δf algorithm assigns to each particle (*marker*), whose dynamics is described by the equations introduced in Sec. 3, a *weight*, expressing the number of particles represented by the marker itself. The kinetic momens are then derived in each cell (labelled by i) of the real space by summing the contribution expressed by the weight of the markers, w_j. This yields to the following expressions for the perturbed density

$$(\tilde{n_e})_i = \sum_{j \in i} (w_j \Delta\Gamma_j^{(c)})/(\Delta\Gamma_i^{(p)}) \ , \tag{12}$$

and the current density

$$\tilde{J} = \sum_{j \in i} (e p_{||j} w_j \Delta\Gamma_j^{(c)})/(m\gamma\Delta\Gamma_i^{(p)}) \ , \tag{13}$$

where $\Gamma_j^{(c)}$ represents the volume in canonical space occupied by marker number j, and $\Gamma_i^{(p)}$ is the volume of the $i-th$ cell in the real space. By the same way, the electron temperature can be obtained as $T_e \equiv p_e/(n_0 + \tilde{n}_e)$, where p_e is the trace of the pressure tensor.

4. Numerical results

Fluid simulations were performed using a grid of 1024×128 points. Periodic boundary conditions along x and y have been imposed both to the fluid and to the test particle codes. In order to carry out a comparison with the cold-ion limit of the reconnection model, we ran two fluid simulations characterized by different values of the (normalized) parameter $\rho_i = 0.2, 0, 4$, while the values of the two parameters d_e and ρ_s have been kept fixed and chosen in such a way to correspond to typical fusion devices parameters. Thus, assuming a characteristic length $L = 10^{-2}$ m, simulations were performed for the (un-normalized) values $d_e = 0.002$ m and $\rho_s = 0.004$ m, corresponding to an equilibrium density $n_0 = 0.710^{19}$ m^{-3} and an electron thermal temperature, $T_e \approx 1.53$ keV, respectively. According to the characteristic evolution time derived from the linear growth rate calculated in the simulations, which is in agreement with the asymptotic formula $\gamma \approx 2(2d_e\rho_\tau^2/\pi)^{1/3}$ ($\rho_\tau^2 = \rho_i^2 + \rho_s^2$) [21], the fluid fields are adequately sampled by saving the output data each 7 Alfvén times for the $\rho_i = 0.2$ simulation and each 5 Alfvén times for the $\rho_i = 0.4$ simulation. With the amplitude of the perturbation adopted in the simulations (10^{-6}), the time required in order to reach the nonlinear phase varies between 110 τ_A for $\rho_i = 0$ and 50 τ_A for $\rho_i = 0.4$, while the saturated phase of the process is attained after 270 τ_A when $\rho_i = 0$ and 190 τ_A when $\rho_i = 0.4$.

The perturbed magnetic flux and the electrostatic potential calculated by the reconnection code are then read by the electron code, which evolves the spatial position, the parallel velocity and the weight of the markers. The results of the electron simulations presented in this paper have been obtained by loading 1×10^7 particles.

A first comparison between the moments provided by the electron simulations and the corresponding fluid quantities confirm a good agreement of the linear growth rate, as shown for the current density in fig. 1.

Similarly to the case $\rho_i = 0$, in the linear phase of the process the parallel electric field provided by the fluid simulations, $E_{||} = -\nabla_{||}\tilde{\Phi} - \partial\tilde{\psi}/\partial t$, exhibits a structure peaked in the X-point region also when $\rho_i > 0$. Differences arise during the nonlinear phase. As shown in fig. 2, when $\rho_i = 0$ the electric field has a positive peak still located at the X-point, whereas it is negative

elsewhere. In the case $\rho_i \neq 0$, instead, the electric field structure exhibits highly positive values along fine spirals inside the magnetic island as well as all along the magnetic island separatrix (fig. 3). This difference suggests that the amount of thermal electrons that could be accelerated by the parallel electric field in the latter case could be larger than the number of accelerated particles in the case $\rho_i = 0$. In the cold-ion limit, in fact, we found that electrons crossing the X-point region start becoming significantly accelerated by the electric field at the end of the nonlinear stage, although this acceleration is not so important as to produce either highly energetic tails or relativistic ones in the electron distribution function [14]. Also for the two considered values of $\rho_i \neq 0$, no energetic electrons are observed during the linear phase and the *parallel* electron temperature, reconstructed according to the procedure described in Sec. 3.1, remains constant until the beginning of the nonlinear phase. At this step, hotter regions appear along the separatrix close to the X-point first, and then elongate along the separatrix, according to the positive electric field, as plotted in figs. 4 and 5. When the process approaches saturation, significantly accelerated electrons are visible also in the denser regions inside the magnetic island. Such a behaviour of the temperature can be related to the positive structures of the electric field that characterize also the inner regions at this step of the process, as shown in figs. 6 and 7. This evolution of the electron temperature, that increases in $\approx 50\%$ in the hottest regions of the magnetic island both for $\rho_i = 0.2$ and $\rho_i = 0.4$, corresponds to a different deformation of the electron distribution function for the two values of ρ_i, drawn in figs. 8 and 9. While the bulk of the electron distribution is considerably smoothed in both cases, the amount of thermal electrons that increase their parallel velocity is larger when $\rho_i = 0.4$, thus giving a more significant contribution to the high energy slopes of the distribution. Although the maximum value of the parallel electric field is similar for both values of ρ_i m, in fact, in the case $\rho_i = 0.4$ this value is nearly uniform along the fine positive spirals inside the island, as well as along the island separatrix, while it characterizes only the region surrounding the X-point when $\rho_i = 0.2$, as can be seen in fig. 10. Therefore, in the latter case only electrons crossing the X-point region undergo the same relevant acceleration that affects all electrons streaming along the highly positive electric field structures when $\rho_i = 0.4$.

5. Conclusions

We have numerically investigated the response of a thermal electron population to the fields developed during collisionless reconnection in plasma regimes where the effects of the electron and ion temperatures are important. In particular, the presence of a finite ion temperature affects the evolution of the electric field parallel to the magnetic field lines during the nonlinear stage of the reconnection process, when highly positive fine structures develop not only along the magnetic separatrix, but in all the area enclosed by the magnetic island. Since this feature becomes more distinct for higher values of the ion temperature, and in order to compare the effects of such structures with those related to the cold-ion limit of the reconnection model, we considered two different values of the ion Larmor radius, corresponding to a ratio between the ion and the electron temperatures equal to 1 and 1/4, respectively. Similarly to the cold-ion case, also for $\rho_i \neq 0$ a visible electron acceleration can be observed after the beginning of the nonlinear phase, when the regions characterized by a larger density and by positive values of the electric field become rapidly hotter than the surrounding areas. This effect is more pronounced towards the saturated stage, when the fine positive structures of the electric field accelerate also the electrons streaming inside the magnetic island. As a result, the distribution function of the electron parallel velocities, initially set as a Maxwellian, is considerably deformed, with a larger amount of energetic electrons produced for the larger value of the ion temperature. Furthermore, the electron temperature, set by the (constant) electron skin depth at the beginning of the simulations, varies up to the 50% of its initial value in the hottest regions of the magnetic island. Although a more refined reconstruction of the electron temperature behaviour would be

obtained only if the kinetic code would feed back its quantities to the fluid reconnection code, these results show that the isothermal assumption is respected during the linear phase of the reconnection process, while the higher the ion temperature is, the most it is violated during the nonlinear phase.

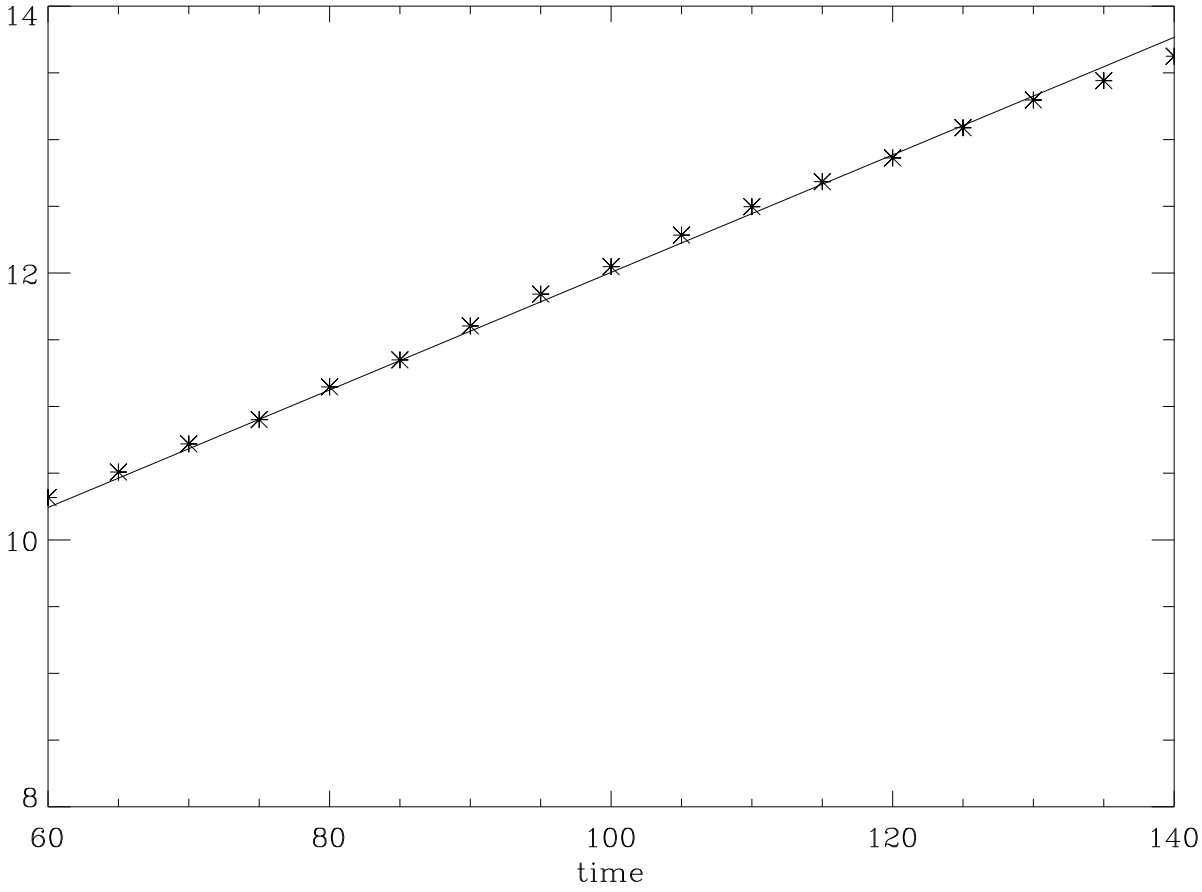

Figure 1. Growth in time of the fluid current density (continuous line) and of the kinetic current density (stars) at the $X-point$ during the linear phase of the reconnection process.

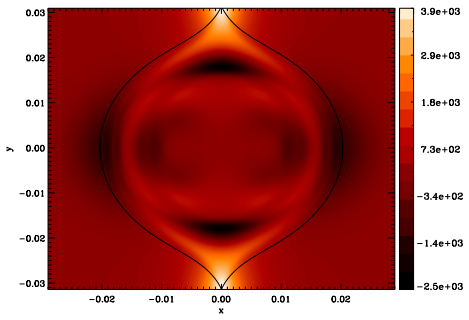

Figure 2. Contour plot of the parallel electric field for $\rho_i = 0$ m.

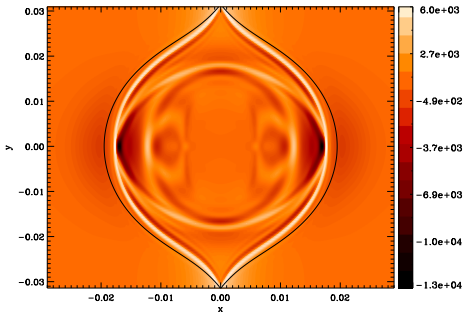

Figure 3. Contour plot of the parallel electric field for $\rho_i = 0.004$ m. The figure is taken at a step of the nonlinear phase of the reconnection process characterized by a width of the magnetic island close to the island width in fig. 2.

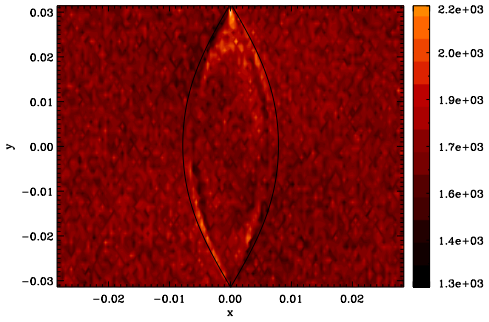

Figure 4. Contour plot of the parallel electron temperature during the nonlinear phase of the reconnection process ($\rho_i = 0.004$ m).

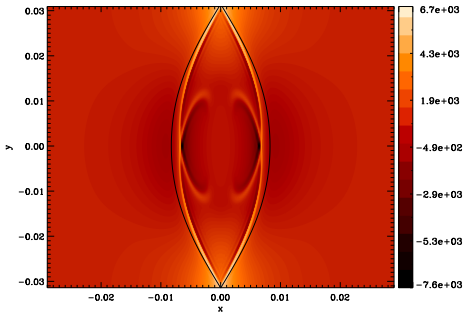

Figure 5. Contour plot of the parallel electric field taken at the same time step of the nonlinear phase of the reconnection process as fig. 4 ($\rho_i = 0.004$ m).

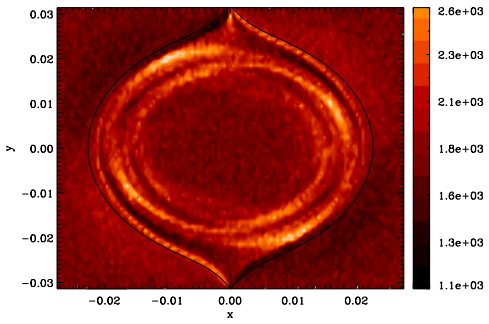

Figure 6. Contour plot of the parallel electron temperature at the saturated stage of reconnection ($\rho_i = 0.004$ m).

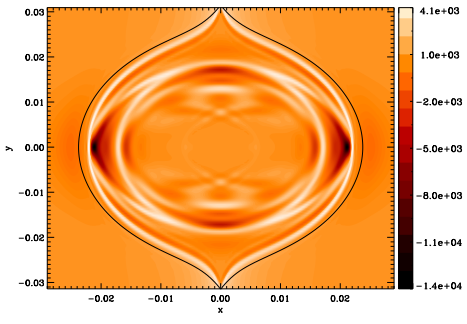

Figure 7. Contour plot of the parallel electric field taken at the same time of the saturated stage of reconnection as fig. 6 ($\rho_i = 0.004$ m).

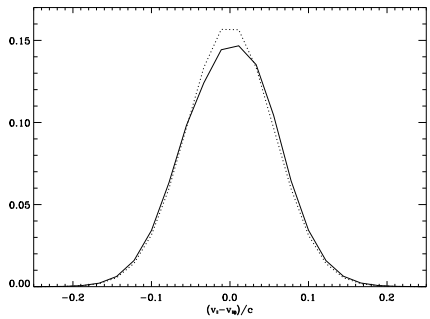

Figure 8. Profile of the distribution function of electrons as function of their parallel velocity normalized to the speed of light (continuos line). The dashed line represents the distribution function at $t = 0$ m. The distribution function refers to the case $\rho_i = 0.002$ m.

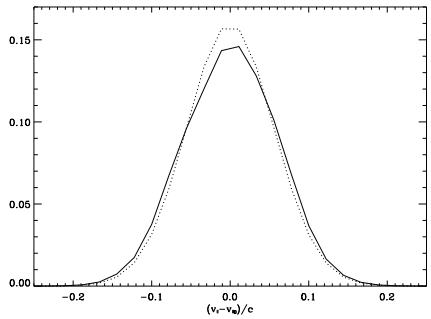

Figure 9. Profile of the distribution function of electrons as function of their parallel velocity normalized to the speed of light (continuos line) The dashed line represents the distribution function at $t = 0$ m. The figure refers to the case $\rho_i = 0.004$ m. As in fig. 8, the distribution function has been normalized to the total number of particles.

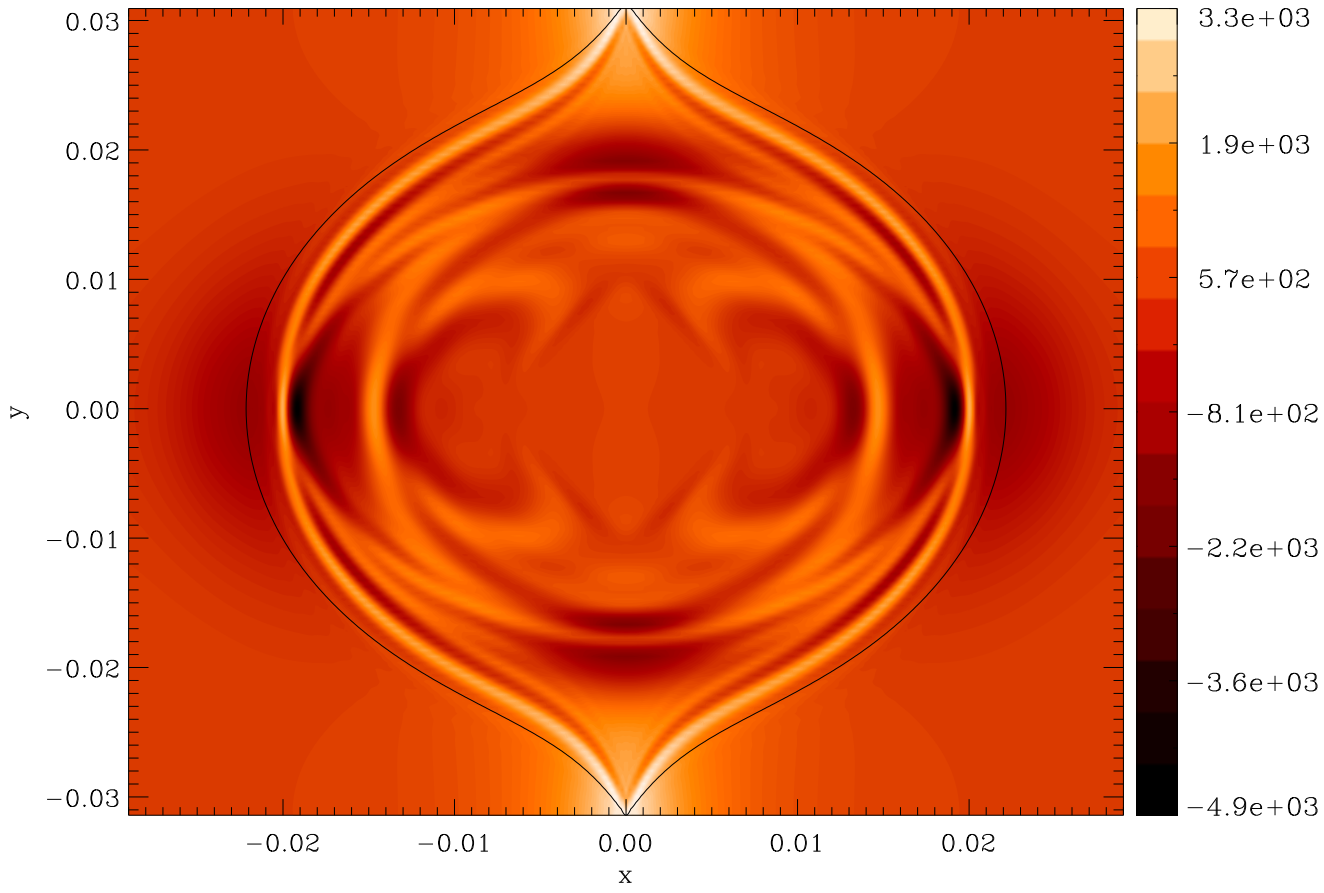

Figure 10. Contour plot of the parallel electric field taken at a step of the reconnection process characterized by an island width close to the island width in fig. 7 ($\rho_i = 0.002$ m).

Acknowledgments
The authors would like to thank dr L-G Eriksson for helpful discussions. This work was partly supported by the Euratom Communities under the contract of Association between EURATOM/ENEA. The views and opinions expressed herein do not necessarily reflect those of the European Commission.

References

[1] Speiser T W 1968 *Earth's Particles and Fields* ed B M McCormac (New York: Reinhold Book Corp.) p. 393.
[2] Savrukhin P V 2001 *Phys. Rev. Lett.* **86** 3036.
[3] Klimanov I, Fasoli A, Goodman T P, and the TCV team 2007 *Plasma Phys. Control. Fusion* **49** L1
[4] Lin R P, Krucker S, Hurford G J, Smith D M, Hudson H S, Holman G D, Schwartz R A, Dennis B R, Share G H, Murphy R J, Emslie A G, Johns-Krull C, and Vilmer N 2003 *The Ap. J.* **595** L69.
[5] Oieroset M, Pin R P, Phan T D, Larson D E, and Bale S D 2002 *Phys. Rev. Lett.* **89** 195001.
[6] Drake J F, Swisdak M, Che H, and Shay M A 2006 *Nature* **443** 553.
[7] Pritchett P L 2006 *J. Geophys. Res.* **111** A10212.
[8] Pritchett P L 2008 *Phys. Plasmas* **15** 102105.
[9] Fu X R, Lu Q M, and Wang S 2006 *Phys. Plasmas* **13** 012309.
[10] Wan W, Lapenta G, Delzanno G L, and Egedal J 2008 *Phys. Plasmas* **15** 032903.
[11] Porcelli F, Borgogno D, Califano F, Grasso D, Ottaviani M, and Pegoraro F 2002 *Plasma Phys. Control. Fusion* **44** B389.
[12] Grasso D, Califano F, Pegoraro F, and Porcelli F 2001 *Phys. Rev. Lett.* **86** 5051.
[13] Grasso D, Pegoraro F, Porcelli F, and Califano F 1999 *Plasma Phys. and Control. Fusion* **41** 1497.
[14] Perona A, Eriksson L-G, and Grasso D 2010 *Phys. Plasmas* **17** 042104.
[15] Waelbroeck F L, Hazeltine R D, and Morrison P J 2009 *Phys. Plasmas* **16** 032109.
[16] Grasso D, Tassi E, and Waelbroeck F L 2010 *Phys. Plasmas* **17**, 082312.
[17] Grasso D, Califano F, Pegoraro F, and Porcelli F 2000 *Plasma Phys. Rep.* **26** 548.
[18] Loureiro N F, and Hammett G W 2008 *J. Comput. Phys.* **86227** 4518.
[19] Brizard A J, and Chan A A 1999 *Phys. Plasmas* **6** 4548.
[20] Candy J 1996 *J. Comput. Phys.* **129** 160.
[21] Porcelli F 1991 *Phys Rev. Lett.* **66** 425.